buildings

Article

Developing and Applying a Double Triangular Damping Device with Equivalent Negative Stiffness for Base-Isolated Buildings

Tianwei Sun [1,2,*], Lingyun Peng [1,*], Xiaojun Li [1] and Yaxi Guan [1]

[1] Beijing Key Lab of Earthquake Engineering and Structural Retrofit, Beijing University of Technology, Beijing 100124, China
[2] Department of Civil Engineering, Tsinghua University, Beijing 100084, China
* Correspondence: tianweisun1990@163.com (T.S.); ply@bjut.edu.cn (L.P.)

Abstract: A passive double triangular damping (DTD) device with equivalent negative stiffness is proposed in this study. The DTD device consists of transmission systems and triangular damping systems. A mechanical model was developed to describe the force–displacement relationship of a triangular damping system, while the feasibility of both the system and model was evaluated using experimental tests. The theoretical analysis demonstrated that DTD was a form of damping with equivalent negative stiffness, and the equivalent expressions were generated. Finally, the prospect of application in the DTD-controlled isolation system was explored using numerical simulation. The results revealed that DTD was more effective than a lead–rubber bearing in reducing isolator displacement and rooftop acceleration when subjected to ground motions.

Keywords: passive; equivalent negative stiffness; triangular damping; numerical simulation; isolation system

Citation: Sun, T.; Peng, L.; Li, X.; Guan, Y. Developing and Applying a Double Triangular Damping Device with Equivalent Negative Stiffness for Base-Isolated Buildings. *Buildings* **2023**, *13*, 3008. https://doi.org/10.3390/buildings13123008

Academic Editors: Xiangyong Ni, Qin Zhang, Weiqing Zhu and Yantai Zhang

Received: 7 November 2023
Revised: 27 November 2023
Accepted: 29 November 2023
Published: 1 December 2023

1. Introduction

Earthquakes are important factors to consider when examining the causes of structural damage or collapse. To improve the seismic performance of real-world structures, methods such as base isolation, energy dissipation devices, high-performance materials, and reinforcement have been applied. As an effective control technology, negative stiffness has received much attention due to the advantages it offers in terms of acceleration control. Researchers have utilized negative stiffness in numerous fields [1–5], such as base isolation, mechanical control, and cable-stayed bridges. To improve the modal damping ratio of the cables in cable-stayed bridges, vibration control techniques with negative stiffness mechanisms have attracted much attention. Viscous damping can be combined with a negative stiffness device in series or in parallel [6,7]. The enhanced displacement response of the damper through negative stiffness increases energy dissipation, thereby improving the damping of the cable [8]. Passive negative stiffness is produced by the compression force of the springs or magnet array, while a semi-active technology using a magnetorheological damper can also achieve negative stiffness [9] by controlling voltage.

In the field of seismic isolation, base isolation is one of the most effective techniques for protecting engineering structures from strong earthquakes [10]. With the aid of isolators, these superstructures can be decoupled from the foundation and their natural fundamental frequencies can be shifted beyond the dominant frequency components of earthquake-induced ground motions [11–13]. Zhen et al. [14] developed a numerical model of the Sliding-LRB, which can effectively predict the hysteretic behavior under cyclic loadings. In addition, a re-centering seismic isolator [15] was developed by combining damping-enhanced sliding lead–rubber bearings with superplastic shape memory alloy. In addition, pendulum isolators with variable stiffness [16], conical friction pendulum isolators [17], and variable friction pendulum isolators [18,19] have been developed to improve the effectiveness of vibration isolation. Studies have demonstrated that low horizontal stiffness of isolators is required for effective vibration isolation when subjected to low-frequency ground motions [20–22]. Palazzo et al. [23] proposed a system that includes a tuned mass damper (TMD) and an isolation device to attenuate the effects of the seismic excitation components with frequencies close to the fundamental natural vibration. Taniguchi et al. [24] proposed the installation of a TMD to reduce the displacement demand on a base-isolated structure. Kapasakalis et al. [25,26] used KDampers with negative stiffness to achieve small base displacements at higher nominal frequencies, which can be used as a supplement to conventional seismic isolation bases. Kalogerakou et al. [27] investigated the possibility of negative stiffness to control vertical seismic motions in isolated structures. Su et al. [28] proposed a negative stiffness TMD-optimized design for testing dynamic and static performance.

Negative stiffness is advantageous [29–33] because it can generate forces in the same direction as the horizontal motion of the isolation layer and reduce the natural frequency of vibration without impacting the bearing capability of the isolator. As a result, technology for base isolation with negative stiffness [34–36] has received great attention. Negative stiffness can be physically realized by pre-compressed springs [37], convex-interface pendulums [38], inerter [39,40], and magnetic mechanisms [41]. With respect to the development of a negative stiffness device, Nepal et al. [42] designed a device with both negative and positive springs to improve current base isolation systems. This device can avoid resonance to achieve controlled displacements and accelerations under various earthquake scenarios. Luo et al. [43] investigated the earthquake resistance of a base-isolated structure with different negative stiffness damping models and proposed a method for designing these models utilizing multi-objective optimization. Through a combination of magnetic negative stiffness spring and eddy current damping, Shan et al. [44] proposed an innovative subsystem with better energy transition behavior to enhance the performance of existing base isolation. Cimellaro et al. [45] presented a three-dimensional isolation system based on a negative stiffness device. This system can change the stiffness of the isolator to model reduced vertical seismic forces. Iemura et al. [46,47] proposed a negative stiffness hysteresis loop to control the seismic response of structures and demonstrated its advantages and effectiveness experimentally. Sun and Peng et al. [48–50] designed several types of devices that exhibit negative stiffness. Through experimental and theoretical methods, Nagarajaiah et al. [51–54] investigated whether the seismic performance of structures can be improved with negative stiffness devices. The results revealed that negative stiffness devices can significantly reduce absolute and relative displacement transmissibility. To generate negative stiffness, Pan [55] proposed a cylindrical structure in which the internal hollow portion is filled by inclined beam elements. Zhang [56] proposed a magnetic negative stiffness isolator to enhance the low-frequency vibration-isolation capability of the system. Finally, Wu [57] proposed a compact magnetic spring with linear negative stiffness to improve the working range of the device in a limited space.

In this paper, a novel double triangular damping device is proposed, which generates double triangular damping (DTD). The device is a new mechanism for passive generation of equivalent negative stiffness compared to existing devices. The DTD is a type of damping with equivalent negative stiffness characteristics as confirmed by frequency response analysis. The development of a DTD device consisting of triangular damping systems and transmission systems is described in detail. Experimental tests of the triangular damping system were conducted to examine its mechanical model. Finally, the numerical simulation of a base isolation system with DTD is evaluated. The increased efficacy of DTD on base isolation is discussed in terms of rooftop acceleration and maximum isolator displacement.

2. Mechanism and Experimental Tests of a Triangular Damping System

If the damping generated in the unloading phase exceeds that of the loading phase, then hysteresis with equivalent negative stiffness can be obtained [50]. To realize this mechanism, a passive triangular damping system was designed.

2.1. Mechanism of the Triangular Damping System

To achieve small damping in the loading phase and large damping in the unloading phase, a triangular damping system was developed, as shown in Figure 1. The system is composed of connecting devices-I and -II, outer tube, lid, sealing rubber ring, counterweight ring, sand, and round bar. The outer tube is filled with sand. A counterweight ring is placed above the sand. The counterweight ring and the lid have a round hole in the middle, which is surrounded by sealing rubber rings. The lower end of the round bar is pre-buried into the sand to a depth of L. The upper end of the round bar passes through the circular holes of the lid and the counterweight ring and is connected to the connecting device-I. Connecting device-II is used to fix the triangular damping system in place.

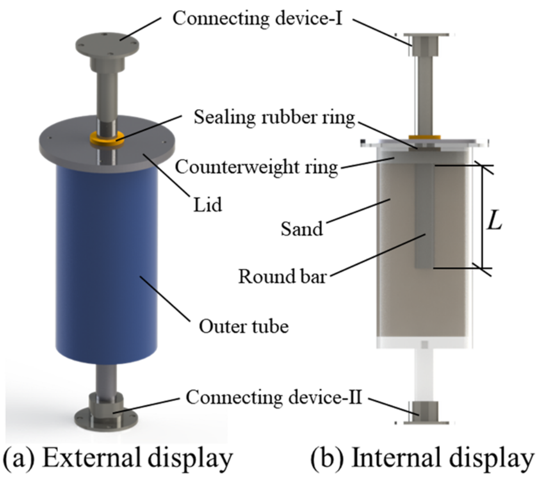

Figure 1. Detailed 3D model of the triangular damping system.

Figure 2a depicts the loading phase of the triangular damping system, where the round bar moves upward and is subjected to skin friction Q_s, as shown in the upward phase of Equation (1). Figure 2b depicts the unloading phase of the triangular damping system, where the round bar moves downward and squeezes the sand, and is subject to the combined action of skin friction Q_s and tip resistance Q_P, as shown in the downward phase of Equation (1). The force Q of the triangular damping system can be expressed as

$$Q = \begin{cases} Q_s & \text{Upward} \\ Q_s + Q_P & \text{Downward} \end{cases} \quad (1)$$

where $Q_s = ulq_{sik}$, $Q_P = Aq_{pk}l/L$; u is the circumference of the round bar; L is the depth of the round bar pre-buried in the sand; l is the depth of the round bar in the sand in the current state; A is the area at the end of the round bar; q_{sik} [58] is the range of standardized values of ultimate lateral resistance of the round bar; q_{pk} is the range of standardized values of ultimate terminal resistance of the round bar.

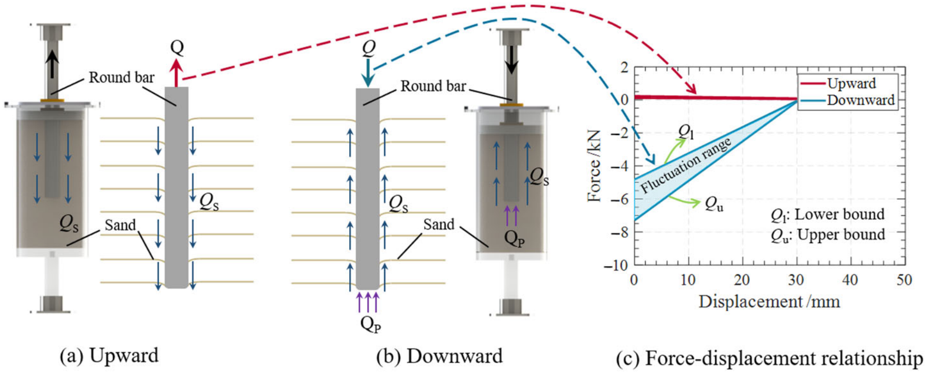

Figure 2. Schematics and working principle of the triangular damping system.

The parameter values presented in Table 1 were set and the displacement–force relationship was plotted using Equation (1), as shown in Figure 2c. During the loading phase, when the round rod moves upward, a very small resisting force is generated. During the unloading phase, as the round rod moves downward, the resisting force that is generated is significantly larger than in the loading phase. In addition, Q_l and Q_u are the lower and upper bounds, respectively, of the Q value during unloading and their values are determined by the range of q_{sik} and q_{pk}.

Table 1. Parameter values of the triangular damping system.

Parameter	u/m	q_{sik}/kPa	A/m^2	L/m	q_{pk}/kPa
Value	0.157	15~30	1.96×10^{-3}	0.05	4000~6000

An important fact to note is that as the round bar moves upward, the sand can quickly self-compact into the gap due to the gravity of the counterweight ring (as depicted in Figure 3). Consequently, the round bar can squeeze the sand directly to create a resisting force as it moves downward.

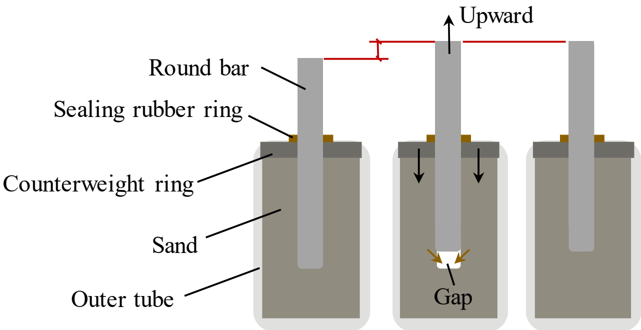

Figure 3. Self-compacting processes of the triangular damping system.

2.2. Experimental Tests of the Triangular Damping System

2.2.1. Experimental Specimen

Figure 4a depicts the experimental specimen of the triangular damping system, which was made of Q345b steel. The inside of the system was filled with compacted sand and the round rod was pre-buried to a depth of 50 mm. The circumference of the round rod was 0.157 m, and its area was 1.96×10^{-3} m. The range of q_{sik} was 15 to 30 kPa and the range of q_{pk} was 4000 to 6000 kPa. The loading test platform produced by Three Units Testing System Company in Beijing, China for testing the mechanical properties of the damper, as shown in Figure 4b, was used in this study as the test platform. The loading facility utilized the PID control method to load the triangular damping system for displacement loading. The axial loading facility performed five quasi-static loading tests of the triangular damping system with a loading displacement magnitude of 30 mm.

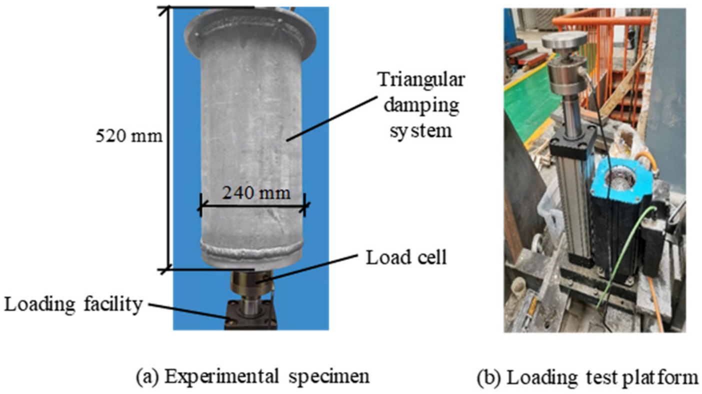

Figure 4. Experimental specimen of the triangular damping system.

2.2.2. Experimental Results

Figure 5 presents a comparison of the experimental and theoretical results (from Equation (1)). The results indicate that the triangular damping system can generate expected hysteresis curve characteristics. Specifically, it generated small resisting forces during the loading phase (i.e., when the round bar moved upward), which is consistent with the theoretical values. During the unloading phase (i.e., when the round bar moved downward), the triangular damping device generated significantly greater resistant forces than during the loading phase.

Notably, the zoomed-in view of the unloading phase shows that the resisting force gradually approached the lower bound of the theoretical value (i.e., Q_l) as the number of loadings increased. This was because the compactness of the sand decreased compared with the initial state, causing the resisting force to decrease. The experimental results demonstrate the feasibility and effectiveness of the triangular damping system.

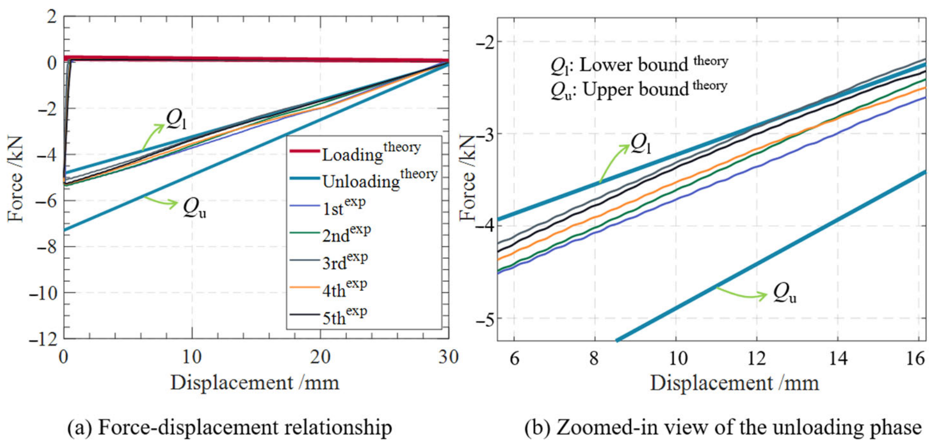

Figure 5. Comparison of experimental and theoretical results of the triangular damping system. (Note: superscript 'exp' represents the experimental result; superscript 'theory' represents the theoretical result; the ordinal numbers represent the sequence of experiments.)

3. Mechanism and Analysis of DTD Device

As explained in Section 2, the triangular damping system generates resisting force only in the positive direction of the x-axis. For the DTD device to generate triangular damping in both the positive and negative directions of the x-axis, a transmission system was designed to work with the triangular damping system.

3.1. Mechanism of the DTD Device

The 3D model of the DTD device is shown in Figure 6a and consists of a connecting device and outer shell, where the connecting device passes through holes preset in the outer shell. In addition, the base of the DTD device and connecting device can be used to secure the structure. Figure 6b shows the interior perspective view of the DTD device, which consists of two symmetrically installed triangular damping systems, a transmission system, and support plates. The support plate holds up the middle part of the connecting rod. Bearings are installed in the support plate to reduce the frictional resistance caused by the rotation of the connecting rod. The zoomed-in view of the interior is shown in Figure 6c; the design of installing gears at the ends of the connecting rod means that the transmission system and the triangular damping system are not in the same vertical plane, which increases the amplitude of the upward movement of the round bar. Refer to Section 3.2 for details on how the transmission system works.

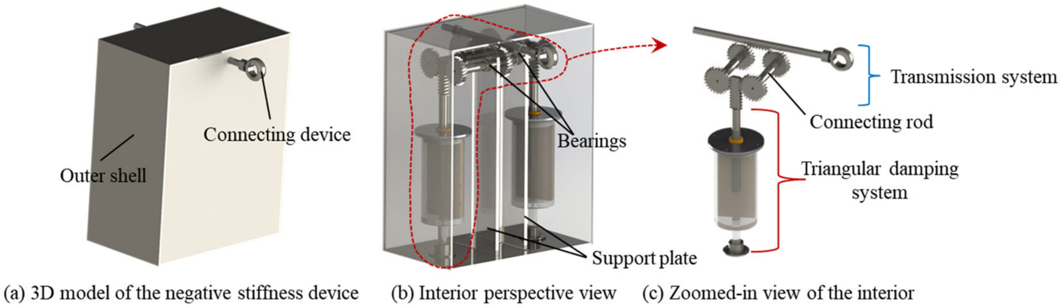

Figure 6. Schematic of the DTD.

3.2. Transmission System

As depicted in Figure 7, the transmission system is composed of a rack, a double-sided rack, gears, linear bearings, outer shell, and a connecting device. Gears are installed on both ends of the double-sided rack, which is connected to the round bar of the triangular damping system. A rack is fixed in the center of the connecting device. The connecting device passes through linear bearings in the outer shell and drives the rack to produce horizontal movement. The gear is rotated by the rack during this horizontal movement, forcing the double-sided rack to move upward or downward. However, the rack only drives one side of the gear when moving in each direction. In summary, the transmission system converts horizontal motion into vertical motion, which drives the operation of the triangular damping system.

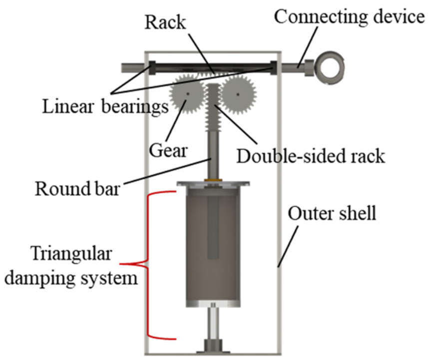

Figure 7. Three-dimensional model of the transmission system.

Assuming that the gear and rack have good transfer efficiency and negligible inertia, and that the meshing of the rack with the left and right gears is stable and instantaneous, the hysteretic curve under one cycle is generated as follows: When the connecting device moves the rack to the right from its initial position, the right gear is made to rotate clockwise, as indicated by the red arrows in Figure 8a. The right gear drives the round bar of the triangular damping system upward through the double-sided rack to generate a small resisting force (i.e., loading I). When the connecting device moves the rack from the right to the initial position, the right gear is rotated counterclockwise which moves the round bar downward, as shown by the blue arrows. The triangular damping device generates an increasing resisting force (i.e., unloading I).

Similarly, when the left gear is rotated by the rack, the round bar is moved upward to generate a small resisting force (i.e., loading II), as indicated by the yellow arrows in Figure 8b. The rack drives the round bar to move downward through the gear, generating an increasing resisting force as it approaches its initial position (i.e., unloading II), as shown by the green arrows.

In summary, through the cooperation of the transmission system and the triangular damping system, the device resisting force is generated, as displayed in Figure 8c, which is named DTD.

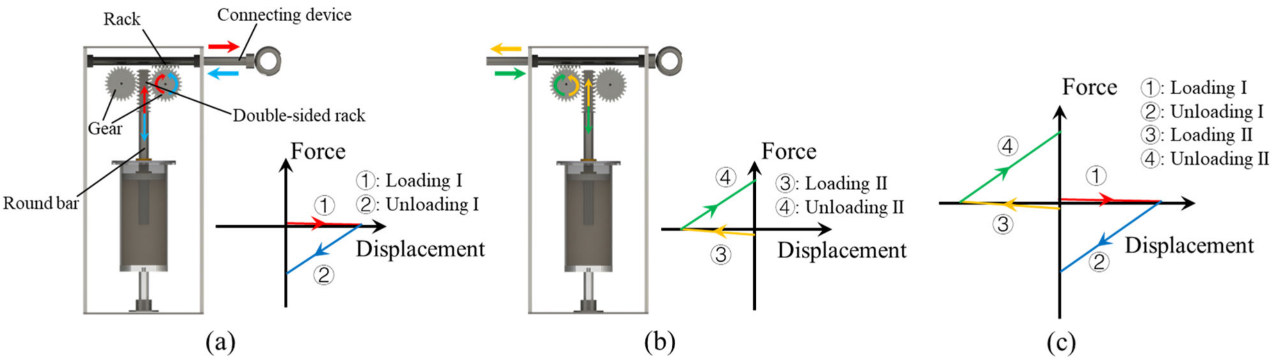

Figure 8. Mechanisms of operation of the transmission system and triangular damping system: (**a**) Rack drives the right gear, and the force-displacement relationship (**b**) Rack drives the left gear, and the force-displacement relationship (**c**) Total force-displacement relationship.

3.3. Hysteresis Characteristic Analysis of the DTD

To further analyze the hysteresis characteristics of the DTD generated by the device, a single-degree-of-freedom (SDOF) system was established, as depicted in Figure 9, where m, k, and c represent the mass, stiffness, and damping coefficient of the SDOF system, respectively. The excitation is denoted by P, and $P = -P_0 \sin(\omega_i t + \theta_i)$, where ω_i, P_0, θ_i, and t represent the excitation frequency, excitation amplitude, phase angle, and time, respectively. $F(x)$ denotes DTD. The SDOF system with DTD obeys the following equation of motion:

$$m\ddot{x} + c\dot{x} + kx + F(x) = P \tag{2}$$

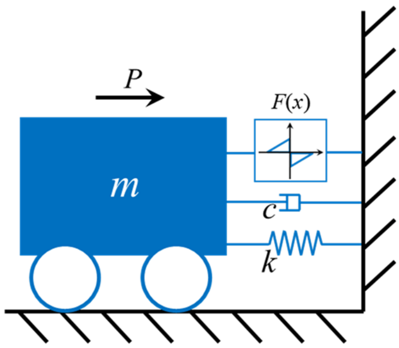

Figure 9. SDOF system with DTD.

If Equation (2) is divided on both sides by k, then in terms of the new parameters $y_s = P_0/k$, $\omega_0 = \sqrt{k/m}$, and $\zeta_0 = c/2m\omega_0$, it can be rewritten as

$$\frac{1}{\omega_0^2}\ddot{x} + \frac{2\zeta_0}{\omega_0}\dot{x} + x + \frac{F(x)}{k} = -y_s \sin(\omega_i t + \theta_i) \tag{3}$$

Assume the steady-state solution of Equation (3) is $x = b\sin\theta$, where $\theta = \omega_i t + \theta_i + \theta_0$, the magnitude is b, and the phase angle is θ_0. If $\eta = \omega_i/\omega_0$, Equation (3) can be rewritten as

$$-\eta^2\sin(\theta) + 2\zeta_0\eta\cos(\theta) + \sin(\theta) + \frac{F(\theta)}{kb} = -\frac{y_s}{b}\sin(\theta - \theta_0) \tag{4}$$

Equation (4) is multiplied on both sides by $\sin\theta$ and $\cos\theta$, respectively. According to trigonometric orthogonality, the expression during one cycle $[0, 2\pi]$ is

$$\begin{cases} \eta^2 - 1 - \frac{1}{\pi kb}\int_{2\pi}^{0} F(\theta)\sin\theta d\theta = \frac{y_s}{b}\cos\theta_0 \\ 2\zeta_0\eta + \frac{1}{\pi kb}\int_{2\pi}^{0} F(\theta)\cos\theta d\theta = \frac{y_s}{b}\sin\theta_0 \end{cases} \tag{5}$$

Furthermore,

$$\left(\eta^2 - 1 - \frac{1}{\pi kb}\int_{2\pi}^{0} F(\theta)\sin\theta d\theta\right)^2 + \left(2\zeta_0\eta + \frac{1}{\pi kb}\int_{2\pi}^{0} F(\theta)\cos\theta d\theta\right)^2 = \left(\frac{y_s}{b}\right)^2 \tag{6}$$

The resistance force of the DTD during one cycle $[0, 2\pi]$ can be expressed as follows:

$$F(\theta) = \begin{cases} 0 & [0, \pi/2] \\ k_d b(\sin\theta - 1) & (\pi/2, \pi] \\ 0 & (\pi, 3\pi/2] \\ k_d b(\sin\theta + 1) & (3\pi/2, 2\pi] \end{cases} \tag{7}$$

where k_d is the stiffness of the unloading phases.

Substituting Equation (7) into Equation (6) to obtain the SDOF system with DTD gives

$$\left(\eta^2 - 1 - \frac{(\pi - 4)}{2\pi}\frac{k_d}{k}\right)^2 + \left(2\zeta_0\eta + \frac{k_d}{k\pi}\right)^2 = \left(\frac{y_s}{b}\right)^2 \tag{8}$$

Assuming ζ_0 = 0 and transforming Equation (8) using Taylor expansion yields

$$\left(\eta^2 - 1 - \frac{(\pi - 4)}{2\pi}\frac{k_d}{k}\right)^2 + \left(\frac{k_d}{k\pi}\right)^2 = \left(\frac{y_s}{b}\right)^2 \tag{9}$$

Defining

$$F(\eta, b) = \left(\eta^2 - 1 - \frac{(\pi - 4)}{2\pi}\frac{k_d}{k}\right)^2 + \left(\frac{k_d}{k\pi}\right)^2 - \left(\frac{y_s}{b}\right)^2 = 0 \tag{10}$$

Allows us to derive the following partial differential equation:

$$\frac{\partial b}{\partial \eta} = -\frac{\partial F/\partial \eta}{\partial F/\partial b} = -\frac{4\eta\left(\eta^2 - 1 - \frac{(\pi-4)}{2\pi}\frac{k_d}{k}\right)}{\partial F/\partial b} \tag{11}$$

When Equation (11) = 0, the resonance of the SDOF system with DTD can be calculated from the following equation:

$$4\eta\left(\eta^2 - 1 - \frac{(\pi - 4)}{2\pi}\frac{k_d}{k}\right) = 0 \tag{12}$$

Substituting $\omega_0 = \sqrt{k/m}$, $\eta = \omega_i/\omega_0$ into Equation (12) gives the stiffness of the SDOF system with the DTD, k_n, as

$$k_n = k + \left(\frac{1}{2} - \frac{2}{\pi}\right)k_d \tag{13}$$

Consequently, the equivalent negative stiffness of DTD, k_{en}, is

$$k_{en} = \left(\frac{1}{2} - \frac{2}{\pi}\right)k_d \tag{14}$$

Based on the equivalent principle of equal displacement and equal hysteresis energy under the premise of resonance [59], the equivalent viscous damping constant of DTD is

$$E = c_{ed}\omega_i \pi b^2 = b^2 k_d \tag{15}$$

where E represents hysteresis energy and c_{ed} indicates the equivalent viscous damping constant of DTD.

Furthermore,

$$c_{ed} = \frac{k_d}{\omega_i \pi} \tag{16}$$

where k_d = 0.2, 0.4, 0.6, 0.8 N/m, k = 1 N/m, ζ_0 = 0.05, and y_s = 0.1 m. The correlation between the displacement response coefficient (b/y_s) and η of the DTD is obtained from Equation (8), as presented in Figure 10. The resonance region of the SDOF system with DTD moves to the left with increasing k_d, i.e., the resonance frequency ω_i decreases. This indicates that DTD can reduce the entire stiffness of the system and that the equivalent negative stiffness value is proportional to k_d, which is consistent with Equation (14). In addition, compared with the uncontrolled SDOF system, DTD with increasing k_d reduces the peak value of frequency response by 38.30%, 55.41%, 65.08%, and 71.31%, respectively. Table 2 presents the theoretical values of c_{ed} based on Equation (16) and the assumed parameters. Moreover, c_{ed} is proportional to the value of k_d, which explains the decrease in the displacement response coefficient for increasing k_d. These values confirm that DTD is a form of damping with equivalent negative stiffness.

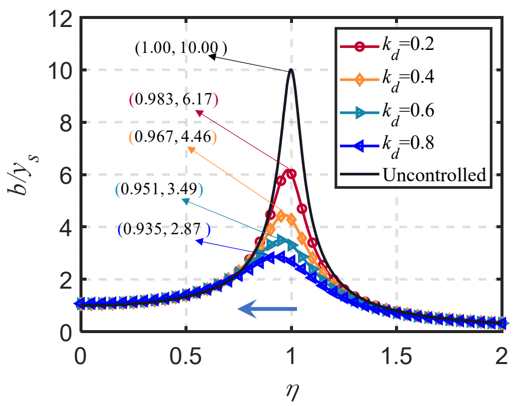

Figure 10. Relationship between displacement response coefficient (b/y_s) and η.

Table 2. The theoretical values of the c_{ed} corresponding to different k_d.

k_d	0.2	0.4	0.6	0.8
c_{ed}	0.065	0.131	0.199	0.270

4. Seismic Control Performance of the DTD Isolation System

4.1. Numerical Example

To verify the performance of the DTD-controlled isolation system, a base-isolated seven-story building frame structure was considered as the prototype for analysis. To simulate the prototype isolation structural system, a lumped mass-and-shear spring model, as shown in Figure 11, was adopted. The prototype building is a Site Class II. The seismic response spectra have a characteristic period of T_g = 0.35 s. The system has lateral stiffnesses of k_s = [1.4, 1.6, 1.5, 1.5, 1.2, 1.5, 0.2] × 10^6 kN/m, heights of

h_s = [4.2, 3.3, 3.3, 3.3, 3.3, 3.3, 4.2] m, lumped masses of m_s = [1.9, 1.8, 1.7, 1.4, 0.8, 0.4, 0.1] $\times 10^6$ kg, and story number s. The total horizontal stiffness, height, damping factor, and the mass of the isolators were $k_0 = 1.2 \times 10^5$ kN/m, h_0 = 2.1 m, $c_0 = 1.1 \times 10^4$ kN/(m/s), and $m_0 = 2.2 \times 10^6$ kg, respectively. The natural period of the base-isolated structure was 1.9 s. The seismic response of the structure was carried out in the SAP2000 program where the inherent damping ratio of the superstructure is taken as 5%.

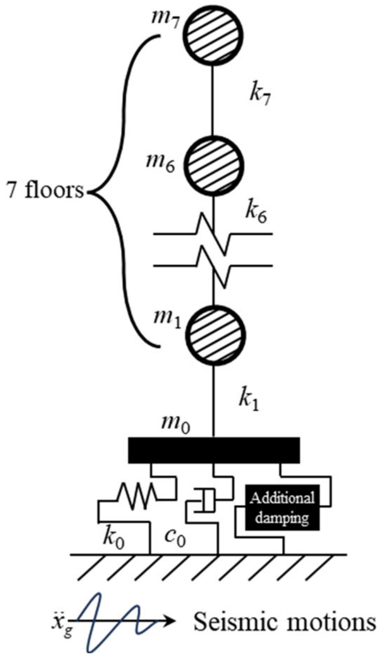

Figure 11. A lumped mass-and-shear spring base-isolated model.

Seven ground motions were selected from the PEER NGA West2 Ground Motion Database [60] to analyze the seismic response of the isolation model. The response spectrum specified in the Chinese code standard for seismic isolation design of buildings (GB 51408–2021 [61]) was used as the target spectrum for ground motion selection. Information on each ground motion record is presented in Table 3. The seismic motions were scaled to a peak ground acceleration of 0.62 g. The response spectra of ground motions are plotted in Figure 12.

Table 3. Information of ground motion records used in the numerical example.

Number	No. in PEER	Year	Mean Square Error	Station Name	Magnitude
NO. 1	392	1983	0.015	Coalinga-14th and Elm (Old CHP)	5.38
NO. 2	1056	1994	0.018	Phelan—Wilson Ranch	6.69
NO. 3	1297	1999	0.017	HWA051	7.62
NO. 4	1499	1999	0.014	TCU060	7.62
NO. 5	3160	1999	0.014	TCU014	6.2
NO. 6	6736	2004	0.015	SIT011	6.63
NO. 7	8855	2008	0.019	Shoshone	5.39

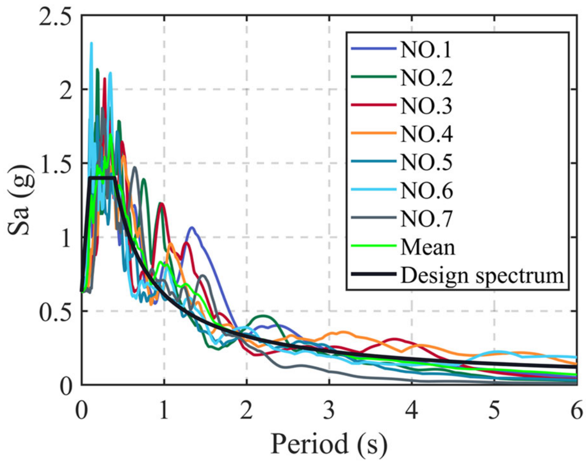

Figure 12. Response spectra of ground motions.

A multilinear elastic element can be used to express the force–displacement relationship with negative stiffness characteristics in SAP2000 [53]. The DTD can be readily implemented in the program SAP2000 using two elements in parallel. The stiffness of Wen plastic element and the multilinear elastic element are connected in parallel to provide the equivalent negative stiffness. As the negative stiffness increases, the additional damping increases to reduce the larger displacement response of the isolation layer due to the reduced stiffness. Therefore, the equivalent negative stiffness provided by the DTD is set to 5% of the stiffness of the isolation layer, reducing the need for additional damping. To improve seismic isolation, DTD devices were installed as additional damping in the isolation layer. Figure 13 depicts the hysteresis curve of the simulated DTD device subjected to ground motion. In addition, the response of a seismic isolation structure with a lead–rubber isolating bearing (LRB) was compared with DTD. The LRB was modeled using a Wen plastic element, which ensured that the energy dissipation of the LRB was comparable to DTD for the same displacement magnitude.

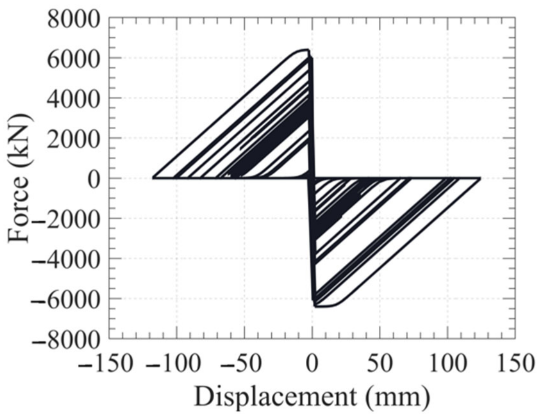

Figure 13. DTD simulation in SPA2000.

4.2. Simulation Results

Figures 14 and 15 illustrate that DTD with an equivalent negative stiffness effect was substantially more effective than the LRB in reducing the maximum rooftop acceleration response and inter-story drifts of the superstructure without compromising maximum isolator displacement. In other words, DTD is more effective in terms of simultaneously reducing isolator displacements and floor response accelerations.

Compared with the LRB-controlled structure, the DTD-controlled structure reduced the maximum isolator displacement and rooftop acceleration responses by averages of 11.96% and 19.30%, respectively, for the seven seismic motions considered. The maximal responses of the different additional damping base-isolated structures are presented in Table 4. Inter-story drifts and rooftop accelerations demonstrate that DTD can enhance the efficiency of conventional isolation techniques and effectively protect the superstructure from ground motions.

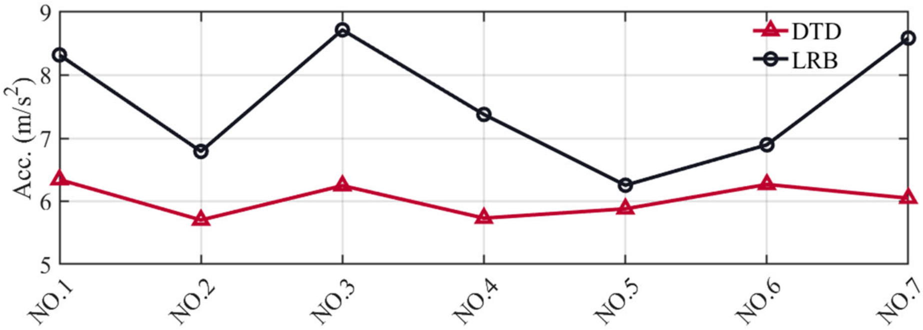

Figure 14. The maximum rooftop acceleration responses of the base-isolated structure underground motions.

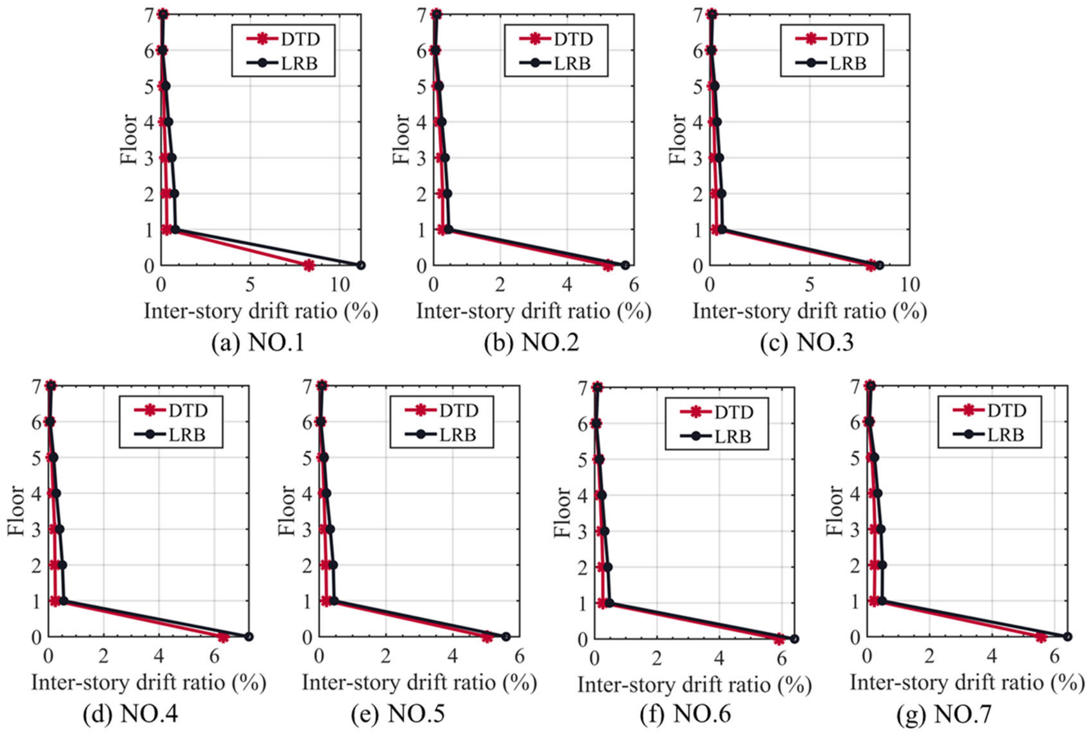

Figure 15. Inter-story drift ratios of the base-isolated structure underground motions.

Table 4. Maximum seismic responses of the base-isolated structure underground motions.

Number	Maximum Isolator Displacement (m)			Maximum Rooftop Acceleration (m/s^2)		
	DTD	**LRB**	**Improvement Rate (%)**	**DTD**	**LRB**	**Improvement Rate (%)**
NO. 1	0.174	0.235	25.97%	6.343	8.321	23.77%
NO. 2	0.110	0.120	8.97%	5.703	6.790	16.02%
NO. 3	0.169	0.178	5.09%	6.248	8.718	28.34%
NO. 4	0.133	0.152	12.79%	5.733	7.377	22.29%
NO. 5	0.106	0.117	10.08%	5.880	6.254	5.98%
NO. 6	0.124	0.134	7.72%	6.267	6.895	9.11%
NO. 7	0.117	0.135	13.13%	6.049	8.589	29.57%

Note: Improvement rate = (LRB − DTD)/LRB.

5. Conclusions

In this work, double triangular damping (DTD) and a specific DTD device are proposed as a means of mitigating seismic damage. To evaluate the DTD vibration control performance, a seven-story isolated building and SDOF were selected as analytical models. Experiments were performed to evaluate the mechanical properties of the triangular damping system. The primary conclusions drawn from this research are as follows:

(1) A passive triangular damping system was proposed. A mechanical model was developed, and its hysteretic behavior was examined using experimental tests, which verified the effectiveness of the proposed triangular damping system.
(2) By coordinating the transmission system with the triangular damping system, an equivalent negative stiffness device was developed, which generated a damping effect named double triangular damping (DTD).
(3) Frequency response analysis of the SDOF system revealed that DTD was able to reduce the natural vibration frequency and control the displacement response of the system. This demonstrated that DTD is a type of damping with equivalent negative stiffness, and the corresponding expressions were presented.
(4) Numerical simulation results revealed that DTD-controlled construction can improve the effectiveness of structural isolation without amplifying the displacement response of the isolation layer. Compared with LRB-controlled structures, DTD-controlled structures reduced the maximum isolator displacement and rooftop acceleration by 11.96% and 19.30%, respectively, on average for the seven seismic motions considered.

Author Contributions: Conceptualization, L.P.; Methodology, T.S.; Software, X.L. and Y.G.; Formal analysis, T.S. and Y.G.; Data curation, L.P.; Writing—original draft, T.S.; Writing—review & editing, L.P.; Visualization, X.L. All authors have read and agreed to the published version of the manuscript.

Funding: The authors gratefully acknowledge the National Natural Science Foundation of China (Grant Nos. 52178098, 51421005), the National Key Research and Development Program of China (Grant No. 2022YFC3003603), and the Postdoctoral funding of Tsinghua University (Grant No. 100408056).

Data Availability Statement: The data presented in this study are available on request from the corresponding author. The data are not publicly available due to this data is obtained through a program that is private and more important.

Conflicts of Interest: The authors declare no conflict of interest.

References

1. Gatti, G.; Brennan, M.J.; Tang, B. Some diverse examples of exploiting the beneficial effects of geometric stiffness nonlinearity. *Mech. Syst. Signal Process.* **2019**, *125*, 4–20. [CrossRef]
2. Hong, N.; Zhao, Z.; Du, Y.; Chen, Q. Energy spectra and performance assessment of isolated structures with a negative stiffness amplification system. *Soil Dyn. Earthq. Eng.* **2023**, *169*, 107857. [CrossRef]
3. Zhang, Y.; Liu, Q.; Lei, Y.; Cao, J.; Liao, W.-H. Halbach high negative stiffness isolator: Modeling and experiments. *Mech. Syst. Signal Process.* **2023**, *188*, 110014. [CrossRef]
4. Dong, G.; Zhang, X.; Xie, S.; Yan, B.; Luo, Y. Simulated and experimental studies on a high-static-low-dynamic stiffness isolator using magnetic negative stiffness spring. *Mech. Syst. Signal Process.* **2017**, *86*, 188–203. [CrossRef]
5. Xu, Y.W.; Xu, Z.D.; Guo, Y.Q.; Huang, X.H.; Zhang, J.; Zhao, Y.L.; Yang, Y.; Zhu, C.; Zhou, M. Single input magnetorheological pseudo negative stiffness control for bridge stay cables. *Smart Mater. Struct.* **2020**, *30*, 015032. [CrossRef]
6. Weber, F.; Boston, C. Clipped viscous damping with negative stiffness for semi-active cable damping. *Smart Mater. Struct.* **2011**, *20*, 045007. [CrossRef]
7. Xu, Y.W.; Xu, Z.D.; Guo, Y.Q.; Zhou, M.; Zhao, Y.L.; Yang, Y.; Dai, J.; Zhang, J.; Zhu, C.; Ji, B.H.; et al. A programmable pseudo negative stiffness control device and its role in stay cable vibration control. *Mech. Syst. Signal Process.* **2022**, *173*, 109054. [CrossRef]
8. Zhou, P.; Liu, M.; Li, H. Optimized negative stiffness damper with flexible support for stay cables. *Struct. Control Health Monit.* **2021**, *28*, e2717. [CrossRef]
9. Høgsberg, J. The role of negative stiffness in semi-active control of magneto-rheological dampers. *Struct. Control Health Monit.* **2011**, *18*, 289–304. [CrossRef]
10. Sato, E.; Furukawa, S.; Kakehi, A.; Nakashima, M. Full-scale shaking table test for examination of safety and functionality of base-isolated medical facilities. *Earthq. Eng. Struct. Dyn.* **2011**, *40*, 1435–1453. [CrossRef]

11. Ibrahim, R.A. Recent advances in nonlinear passive vibration isolators. *J. Sound Vib.* **2008**, *314*, 371–452. [CrossRef]
12. Lu, L.Y.; Lin, G.L. Improvement of near-fault seismic isolation using a resettable variable stiffness damper. *Eng. Struct.* **2009**, *31*, 2097–2114. [CrossRef]
13. Efstathiades, G.J.; Williams, C.J.H. Vibration isolation using non-linear springs. *Int. J. Mech. Sci.* **1967**, *9*, 27–44. [CrossRef]
14. Zheng, W.; Wang, H.; Tan, P.; Li, J.; Liu, Y. Numerical modeling and experimental validation of Sliding-LRBs considering hysteretic strength degradation. *Eng. Struct.* **2022**, *262*, 114374. [CrossRef]
15. Zheng, W.; Tan, P.; Zhang, Z.; Wang, H.; Sun, Z. Damping enhanced novel re-centering seismic isolator incorporating superelastic SMA for response control of bridges under near-fault earthquakes. *Smart Mater. Struct.* **2022**, *31*, 065015. [CrossRef]
16. Zheng, W.; Tan, P.; Li, J.; Wang, H.; Liu, Y.; Yang, K. Seismic performance upgrading of bridges using superelastic pendulum isolators with variable stiffness considering temperature effects. *Eng. Struct.* **2023**, *275*, 115244. [CrossRef]
17. Shang, J.; Tan, P.; Zhang, Y.; Han, J.; Qin, J. Experimental and analytical investigation of variable friction pendulum isolator. *Eng. Struct.* **2021**, *243*, 112575. [CrossRef]
18. Zheng, W.; Tan, P.; Li, J.; Wang, H.; Liu, Y.; Xian, Z. Superelastic conical friction pendulum isolator for seismic isolation of bridges under near-fault ground motions. *Struct. Control. Health Monit.* **2023**, *2023*, 5497731. [CrossRef]
19. Zheng, W.; Tan, P.; Li, J.; Wang, H.; Liu, Y.; Xian, Z. Superelastic pendulum isolator with multi-stage variable curvature for seismic resilience enhancement of cold-regional bridges. *Eng. Struct.* **2023**, *284*, 115960. [CrossRef]
20. Chen, X.; Ikago, K.; Guan, Z.; Li, J.; Wang, X. Lead-rubber-bearing with negative stiffness springs (LRB-NS) for base-isolation seismic design of resilient bridges: A theoretical feasibility study. *Eng. Struct.* **2022**, *266*, 114601. [CrossRef]
21. Zheng, W.; Tan, P.; Liu, Y.; Wang, H.; Chen, H. Multi-stage superelastic variable stiffness pendulum isolation system for seismic response control of bridges under near-fault earthquakes. *Struct. Control Health Monit.* **2022**, *29*, e3114. [CrossRef]
22. Chen, Q.; Hong, N.; Zhang, T.; Zhao, Z. Experiment-based performance evaluation framework for isolated structures in underground subway station-soil-aboveground structure interaction system under seismic excitations. *J. Build. Eng.* **2022**, *56*, 104790. [CrossRef]
23. Palazzo, B.; Petti, L.; de Ligio, M. Response of base isolated systems equipped with tuned mass dampers to random excitations. *J. Struct. Control* **2007**, *4*, 9–22. [CrossRef]
24. Taniguchi, T.; Der Kiureghian, A.; Melkumyan, M. Effect of tuned mass damper on displacement demand of base-isolated structures. *Eng. Struct.* **2008**, *30*, 3478–3488. [CrossRef]
25. Kapasakalis, K.A.; Antoniadis, I.A.; Sapountzakis, E.J. Performance assessment of the KDamper as a seismic absorption base. *Struct. Control Health Monit.* **2020**, *27*, e2482. [CrossRef]
26. Kapasakalis, K.A.; Antoniadis, I.A.; Sapountzakis, E.J. Constrained optimal design of seismic base absorbers based on an extended KDamper concept. *Eng. Struct.* **2021**, *226*, 111312. [CrossRef]
27. Kalogerakou, M.E.; Kapasakalis, K.A.; Antoniadis, I.A.; Sapountzakis, E.J. Vertical seismic protection of structures with inerter-based negative stiffness absorbers. *Bull. Earthq. Eng.* **2022**, *21*, 1439–1480. [CrossRef]
28. Su, N.; Bian, J.; Peng, S.; Chen, Z.; Xia, Y. Balancing static and dynamic performances of TMD with negative stiffness. *Int. J. Mech. Sci.* **2023**, *243*, 108068. [CrossRef]
29. Zhou, S.; Jean-Mistral, C.; Chesne, S. Closed-form solutions to optimal parameters of dynamic vibration absorbers with negative stiffness under harmonic and transient excitation. *Int. J. Mech. Sci.* **2019**, *157–158*, 528–541. [CrossRef]
30. Wang, M.; Sun, F.F.; Nagarajaiah, S. Simplified optimal design of MDOF structures with negative stiffness amplifying dampers based on effective damping. *Struct. Des. Tall Spec. Build.* **2019**, *28*, e1664. [CrossRef]
31. Walsh, K.K.; Sallar, G.; Haftman, J.T.; Steinberg, E.P. Resetting passive stiffness damper with passive negative stiffness device for seismic protection of structures. *Struct. Control Health Monit.* **2021**, *28*, e2774. [CrossRef]
32. Chen, L.; Liu, Z.; Zou, Y.; Wang, M.; Nagarajaiah, S.; Sun, F.; Sun, L. Practical negative stiffness device with viscoelastic damper in parallel or series configuration for cable damping improvement. *J. Sound Vib.* **2023**, *560*, 117757. [CrossRef]
33. Chen, P.; Wang, B.; Dai, K.; Li, T. Analytical and numerical investigations of base isolation system with negative stiffness devices. *Eng. Struct.* **2022**, *268*, 114799. [CrossRef]
34. Li, H.; Li, Y.; Li, J. Negative stiffness devices for vibration isolation applications: A review. *Adv. Struct. Eng.* **2020**, *23*, 1739–1755. [CrossRef]
35. Chowdhury, S.; Banerjee, A.; Adhikari, S. Optimal negative stiffness inertial-amplifier-base-isolators: Exact closed-form expressions. *Int. J. Mech. Sci.* **2022**, *218*, 107044. [CrossRef]
36. Yu, C.; Fu, Q.; Zhang, J.; Zhang, N. The vibration isolation characteristics of torsion bar spring with negative stiffness structure. *Mech. Syst. Signal Process.* **2022**, *180*, 109378. [CrossRef]
37. Pasala, D.T.R.; Sarlis, A.A.; Reinhorn, A.M.; Nagarajaiah, S.; Constantinou, M.C.; Taylor, D. Simulated bilinear elastic behavior in a SDOF elastic structure using negative stiffness device: Experimental and analytical study. *J. Struct. Eng.* **2014**, *140*, 04013049. [CrossRef]
38. Iemura, H.; Pradono, M.H. Advances in the development of pseudo-negative-stiffness dampers for seismic response control. *Struct. Control Health Monit.* **2009**, *16*, 784–799. [CrossRef]
39. Li, H.; Bi, K.; Hao, H. Effect of negative stiffness nonlinearity on the vibration control effectiveness of tuned negative stiffness inerter damper. *Eng. Struct.* **2023**, *293*, 116641. [CrossRef]

40. Jia, R.; Ji, X.; Cheng, Y.; Ikago, K. Seismic response control of core wall structures using tuned viscous mass damper (TVMD) outriggers. *Eng. Struct.* **2023**, *292*, 116546. [CrossRef]
41. Yuan, S.; Sun, Y.; Wang, M.; Ding, J.; Zhao, J.; Huang, Y.; Peng, Y.; Xie, S.; Luo, J.; Pu, H.; et al. Tunable negative stiffness spring using Maxwell normal stress. *Int. J. Mech. Sci.* **2021**, *193*, 106127. [CrossRef]
42. Nepal, S.; Saitoh, M. Improving the performance of conventional base isolation systems by an external variable negative stiffness device under near-fault and long-period ground motions. *Earthq. Eng. Eng. Vib.* **2020**, *19*, 985–1003. [CrossRef]
43. Luo, H.; Zhu, H.; Ikago, K. Optimal design of negative-stiffness dampers for improved efficiency of structural seismic isolation. *J. Build. Eng.* **2023**, *68*, 106172. [CrossRef]
44. Shan, J.; Shi, Z.; Gong, N.; Shi, W. Performance improvement of base isolation systems by incorporating eddy current damping and magnetic spring under earthquakes. *Struct. Control Health Monit.* **2020**, *27*, e2524. [CrossRef]
45. Cimellaro, G.P.; Domaneschi, M.; Warn, G. Three-dimensional base isolation using vertical negative stiffness devices. *J. Earthq. Eng.* **2020**, *24*, 2004–2032. [CrossRef]
46. Pradono, M.H.; Iemura, H.; Igarashi, A.; Toyooka, A.; Kalantari, A. Passively controlled MR damper in the benchmark structural control problem for seismically excited highway bridge. *Struct. Control Health Monit.* **2009**, *16*, 626–638. [CrossRef]
47. Iemura, H.; Igarashi, A.; Pradono, M.H.; Kalantari, A. Negative stiffness friction damping for seismically isolated structures. *Struct. Control Health Monit.* **2006**, *13*, 775–791. [CrossRef]
48. Sun, T.W.; Peng, L.Y.; Li, X.J.; Kang, Y.J.; Deng, Y.K. Development and analysis of negative stiffness friction damping device. *KSCE J. Civ. Eng.* **2021**, *25*, 2587–2602. [CrossRef]
49. Sun, T.W.; Peng, L.Y.; Ji, X.D.; Li, X.J. Development of a negative stiffness friction damping device with an amplification mechanism. *Eng. Struct.* **2023**, *275*, 115286. [CrossRef]
50. Sun, T.W.; Peng, L.Y.; Ji, X.D.; Li, X.J. A Half-Cycle Negative-Stiffness Damping Model and Device Development. *Struct. Control Health Monit.* **2023**, *2023*, 4680105. [CrossRef]
51. Nagarajaiah, S.; Sen, D. Apparent-weakening by adaptive passive stiffness shaping along the height of multistory building using negative stiffness devices and dampers for seismic protection. *Eng. Struct.* **2020**, *220*, 110754. [CrossRef]
52. Pasala, D.T.R.; Sarlis, A.A.; Nagarajaiah, S.; Reinhorn, A.M.; Constantinou, M.C.; Taylor, D. Adaptive negative stiffness: New structural modification approach for seismic protection. *J. Struct. Eng.* **2013**, *139*, 1112–1123. [CrossRef]
53. Sarlis, A.A.; Pasala, D.T.R.; Constantinou, M.C.; Reinhorn, A.M.; Nagarajaiah, S.; Taylor, D.P. Negative stiffness device for seismic protection of structures. *J. Struct. Eng.* **2013**, *139*, 1124–1133. [CrossRef]
54. Nagarajaiah, S.; Zou, K.; Herkal, S. Reduction of transmissibility and increase in efficacy of vibration isolation using negative stiffness device with enhanced damping. *Struct. Control Health Monit.* **2022**, *29*, e3081. [CrossRef]
55. Pan, Y.; Zhou, Y.; Wang, M.; Gao, Q.; Sun, B. A novel reinforced cylindrical negative stiffness metamaterial for shock isolation: Analysis and application. *Int. J. Solids Struct.* **2023**, *27*, 112391. [CrossRef]
56. Zhang, F.; Shao, S.; Tian, Z.; Xu, M.; Xie, S. Active-passive hybrid vibration isolation with magnetic negative stiffness isolator based on Maxwell normal stress. *Mech. Syst. Signal Process.* **2019**, *123*, 244–263. [CrossRef]
57. Wu, M.; Wu, J.; Che, J.; Gao, R.; Chen, X.; Li, X.; Zeng, L.; Jiang, W. Analysis and experiment of a novel compact magnetic spring with high linear negative stiffness. *Mech. Syst. Signal Process.* **2023**, *198*, 110387. [CrossRef]
58. *JGJ 106-2014*; Technical Code for Testing of Building Foundation Piles. China Architecture & Building Press: Beijing, China, 2014. (In Chinese)
59. Li, S.; Wei, B.; Tan, H.; Li, C.; Zhao, X. Equivalence of friction and viscous damping in a spring-friction system with concave friction distribution. *J. Test. Eval.* **2021**, *49*, 20190885. [CrossRef]
60. PEER. *NGA-West2 Database*; Report No. 2013/03; Pacific Earthquake Engineering Research Center: Berkeley, CA, USA, 2013.
61. *GB/T 51408-2021*; Standard for Seismic Isolation Design of Building. China Architecture & Building Press: Beijing, China, 2021. (In Chinese)